Volume 5 | Number 14 | 14 April 2017 | Pages 3417–3632

Journal of Materials Chemistry C

Materials for optical, magnetic and electronic devices

rsc.li/materials-c

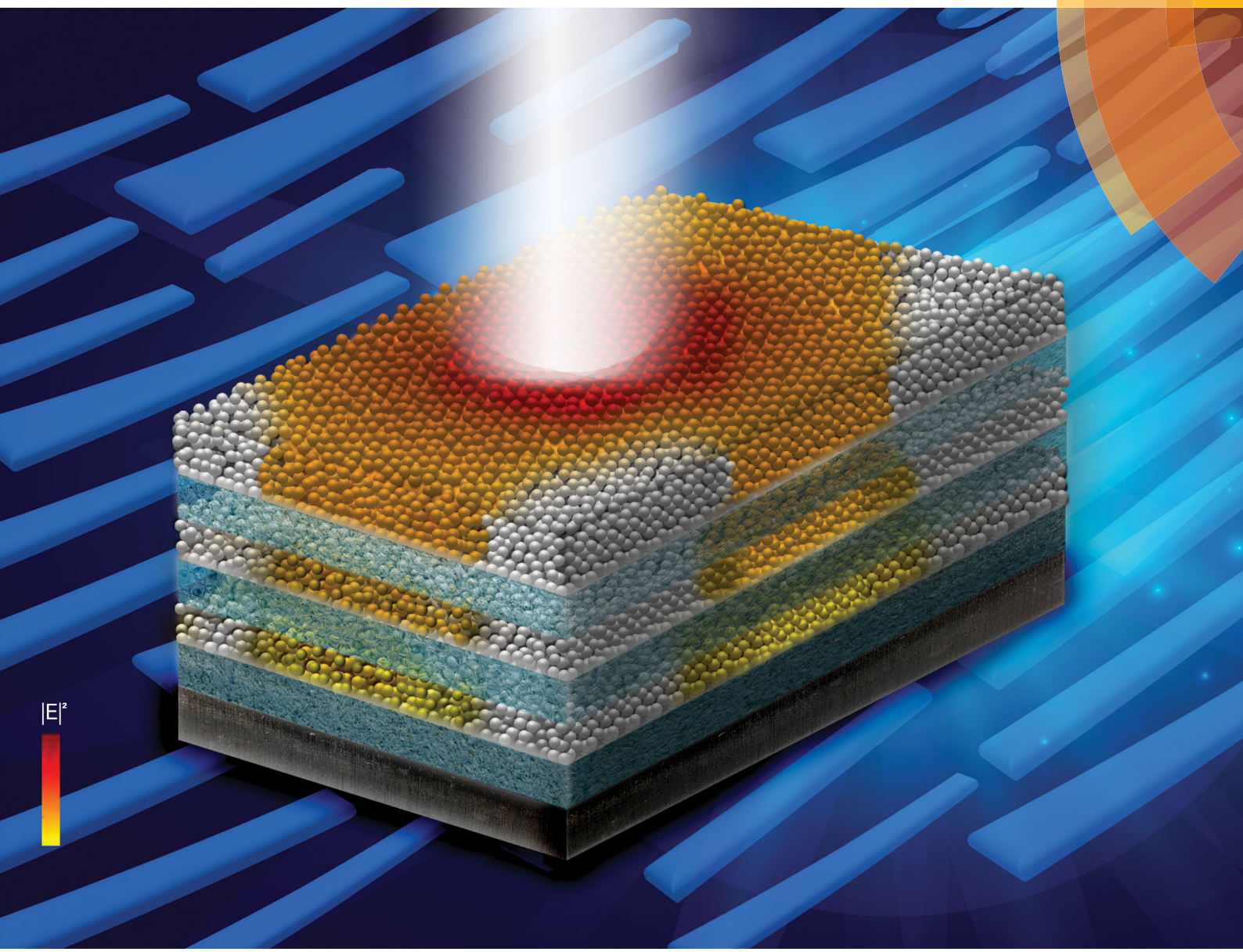

ISSN 2050-7526

ROYAL SOCIETY OF CHEMISTRY

PAPER

Galo J. A. A. Soler-Illia, María Luz Martínez Ricci *et al.*

Designed nanoparticle–mesoporous multilayer nanocomposites as tunable plasmonic–photonic architectures for electromagnetic field enhancement

Journal of Materials Chemistry C

PAPER

Cite this: J. Mater. Chem. C, 2017, 5, 3445

Designed nanoparticle–mesoporous multilayer nanocomposites as tunable plasmonic–photonic architectures for electromagnetic field enhancement†

Rodrigo Martínez Gazoni,[a] Martín G. Bellino,[ab] M. Cecilia Fuertes,[ac] Gustavo Giménez,[d] Galo J. A. A. Soler-Illia*[ef] and María Luz Martínez Ricci*[g]

Received 30th November 2016, Accepted 10th February 2017

DOI: 10.1039/c6tc05195b

rsc.li/materials-c

In this work we present the designed production of a highly tunable nanocomposite able to confine and enhance the electromagnetic field through the combined effects of photonic and plasmonic responses. Silver nanoparticles (NPs) were embedded within a Mesoporous Photonic Crystal (MPC) composed of a mesoporous multilayer presenting a TiO_2–SiO_2 unit cell. This nanosystem was synthesized by a combination of reproducible sol–gel thin film techniques with the selective production of NPs within the titania layers. The design of the MPC architecture was tuned so that each photonic band gap edge would match the plasmonic absorption peak of the Ag NP, in order to combine their confined plasmonic enhancement with that of the band gap edges due to the multilayer structure. We find that the MPC contributes to enhancing the Surface Enhanced Raman Scattering (SERS) signal of probe molecules trapped in the mesopores. This effect indicates the relevance of the unit cell interfaces for the local electromagnetic field enhancements, and opens the gate to performing plasmon-assisted SERS sensing. The resulting material results in a promising platform to study the interplay between photonic and plasmonic systems. These tuneable nano-architectures are highly robust, reproducible, and can lead to applications in sensing platforms, as well as in optoelectronics, enhanced photocatalysis, or artificial photosynthesis.

1. Introduction

Photonic crystals (PCs) are optical structures comprised of a periodic arrangement of dielectric materials with alternate high and low refractive indices. When illuminated with an electromagnetic wave propagating along certain directions, these structures present spectral regions of forbidden transmittance at well-defined frequency ranges called photonic band gaps (PBGs).[1,2] As a result of multiple Bragg's interference, the PBG depends on the geometric and constitutive parameters of the PC structure, such as the lattice size and the refractive index contrast. The one-dimensional photonic crystal (1D-PC), also known as the Bragg reflector, consists of a periodic multilayer comprising two (or more) alternating slabs of conventional dielectric materials. A wide range of materials and processes have been used to construct 1D-PC, including classical sol–gel derived oxides,[3] nanoparticles[4] or self-assembled polymers.[5,6] Possibilities were widened when mesoporous dielectric materials started to be used for the design of artificial PCs, since the presence of accessible mesopores within the dielectric slabs allowed exploring the vapour sensing potential of these structures.[7,8] These results led to the growing field of Mesoporous PCs (MPCs).

The reproducible fabrication of MPCs relies on the controlled synthesis of mesoporous thin films (MTFs). Several methods have been employed to this end, some of which include the deposition of nanoparticles,[9,10] electrochemical etching,[11] or glancing

[a] Gerencia Química, Centro Atómico Constituyentes, Comisión Nacional de Energía Atómica, Avenida General Paz 1499, B1428KNA, San Martín, Argentina
[b] Departamento de Micro y Nanotecnología, Centro Atómico Constituyentes, Comisión Nacional de Energía Atómica, Avenida General Paz 1499, B1428KNA, San Martín, Argentina
[c] Instituto Sábato, UNSAM-CNEA, Avenida General Paz 1499, B1428KNA, San Martín, Argentina
[d] CNMB, Instituto Nacional de Tecnología Industrial, Avenida General Paz 5445, B1650WAB, San Martín, Argentina
[e] DQIAQF, Facultad de Ciencias Exactas y Naturales, Universidad de Buenos Aires, Ciudad Universitaria, Pab. II, C1428EHA, Ciudad Autónoma de Buenos Aires, Argentina
[f] Instituto de Nanosistemas, Universidad Nacional de General San Martín, Av. 25 de Mayo y Francia, 1650, San Martín, Argentina. E-mail: gsoler-illia@unsam.edu.ar; Tel: +54 11 2033-1400, ext 6036
[g] INQUIMAE, Facultad de Ciencias Exactas y Naturales, Universidad de Buenos Aires, Ciudad Universitaria, Pab. II, C1428EHA, Ciudad Autónoma de Buenos Aires, Argentina. E-mail: mricci@qi.fcen.uba.ar; Tel: +54 11 4576-3378

† Electronic supplementary information (ESI) available. See DOI: 10.1039/c6tc05195b

angle vapor physical deposition.[12] Evaporation-Induced Self Assembly (EISA) is a versatile technique to obtain MTFs with controlled pore size and high optical quality.[13–15] When stacking alternating MTF oxide layers (*e.g.*: SiO_2, TiO_2, or even polymers) in periodic unit cells, MPCs with high reflectivity are obtained.[7,8,16] One of the most interesting aspects of these MPCs is the possibility of accessing the interconnected pores of each layer. It has already been proved that a multilayer exposed to a saturated solvent atmosphere presents significant changes in the PBG position and intensity, due to solvent adsorption in the mesopores. The final optical response is due to the increase in the average refractive index of each layer (which shifts the reflectivity to longer wavelengths) upon adsorbing the vapour and the loss of optical contrast, which results in the decrease of the reflectivity.[17] This responsive character of MPCs makes them particularly interesting for sensor applications.[8,18–20] In addition, by tuning the porosity, refractive index and/or the sequence of mesoporous thin films, optical defects can be induced to attain optical resonators responsive to molecular size.[21] MPCs have also been recently integrated in more complex optical devices such as Tamm resonators with potential sensing ability[2] or optical resonators integrating nano-species such as colloidal semiconductor quantum dots.[22]

In the last decade, MTFs have been extensively studied due to the possibility of tailoring several morphological parameters that permit to finely tune their optical and surface properties. The possibility to functionalize the pores with organic groups,[8,23,24] or to confine metallic[25–27] or semiconductor[28,29] nanoparticles (NPs) inside them, enlarges the diverse optical responses of the films. This opens a wealth of possibilities that rely on the combination of photonics, plasmonics and/or quantum size effects to create responsive architectures of tailorable complexity with applications in photovoltaics,[30] optoelectronic devices[31] or sensing. MPCs are indeed the first milestone towards sophisticated photonic noses.[32]

The combination of MPCs with metallic NPs in a spatially controlled manner benefits from the synergy of the photonic and plasmonic features of a NP–MPC nanocomposite. The optical response of metal NPs is characterized by the presence of an important absorption peak due to the Localized Surface Plasmon Resonance (LSPR). The characteristics of this absorption peak are linked to the NP size, shape and the dielectric medium surrounding it.[33] At the plasmon resonance, the electromagnetic energy is confined near the surface of the NP and decays rapidly at distances much smaller than the resonance wavelength. This strong localization of the enhanced electric field has been extensively exploited in different types of sensor devices. In particular, the incorporation of metallic NPs in MTFs has been proved to be a robust, low-cost and reproducible SERS active substrate with potential in selective molecule sieving.[34–36] The possibility of using EM fields enhanced and confined by an MPC to excite plasmon resonances of NPs would open the path towards new devices, useful for surface-enhanced Raman spectroscopy (SERS) or surface plasmon-amplified catalysis.[37–39]

In order to design these complex plasmonic–photonic nano-systems, it is essential to precisely control the positioning of the metallic NP within a well-defined region of the mesoporous multilayer. Several methods, such as direct self-assembly using core–shell $Au@SiO_2$ nanoparticles, have been developed to synthesize these NP–mesoporous multilayer architectures.[40,41] Our group has demonstrated that MTFs can be used as selective nano-reactors for the *in situ* synthesis of well-localized Ag NPs. Light-induced photoreduction of Ag^+ in mesoporous titania in the presence of ethanol leads to producing Ag^0 NP patterns within the mesopores.[42] This lithography-assisted process can be easily controlled in order to tune the contents of silver NPs within the mesopores, leading to conductive nanocomposites.[43] In addition, soft reduction of Ag^+ ions with formaldehyde leads to Ag NP localization in the titania layers of a silica–titania multilayer, while keeping the mesopores accessible. This demonstrates that a clear chemical selectivity between SiO_2 and TiO_2 layers can be attained.[44] Consequently, the possibility of selectively embedding metallic NPs inside the pores of the PC layers opens up the possibility of obtaining a new set of optical responses due to a photonic–plasmonic interaction.

In this work we present the designed production of a nanocomposite multilayer architecture, able to control the electromagnetic (EM) density field enhancement and spatial location. For this purpose, one-dimensional multilayer MPCs were designed and synthesized, aiming at tuning their band gap edges with the LSPR position of silver nanoparticles infiltrated in the multilayer. These NP–MPC structures are expected to enhance the EM field as a dual-consequence of the periodicity of the photonic crystal architecture and the plasmon resonance. To achieve this objective, mesoporous SiO_2–TiO_2 multilayers were first numerically designed and then synthesized by a successive dip-coating process. It is important to remark that the electric permittivity – $\varepsilon(\lambda)$ – of the periodic structure layers used for the numerical simulations was accurately measured by ellipsometry, thus ensuring an optimal modelling of the optical response of these complex systems. The 1D-MPCs were then infiltrated with Ag^+, followed by mild reduction that leads to very well-defined localization of Ag NPs in the TiO_2 layers. The EM field distribution was simulated to assess its spatial localization. Raman studies using an active probe (thiopyridyne) were carried out to monitor the EM field. An increase in the enhancement of the thiopyridyne Raman signals was observed in the NP@MPC systems, which was several times higher than the one obtained with Ag NP embedded in mesoporous films with equivalent thickness and Ag loading. The combined photonic–plasmonic effect observed proves that NP@MPC structures lead to an extra enhancement due to the photonic structure, and opens the gate to SERS-active substrates with an enhanced signal.

2. Experimental section

Chemicals & synthesis of MPCs

MPCs were prepared on silicon substrates by alternating deposition of silica and titania layers, using the EISA approach in a

sequential fashion.[8,45,46] Each MTF was prepared from absolute ethanol–water solutions. Tetraethyl orthosilicate (TEOS-Aldrich) and $TiCl_4$ (Fluka) were used as inorganic precursors, and cethyltrimethyl ammonium bromide (CTAB-Aldrich) or Pluronics F127 $(EO)_{106}(PO)_{70}(EO)_{106}$ (Aldrich) were chosen as pore templates. The final molar ratio compositions for the initial solutions were: TEOS : EtOH : H_2O : HCl : CTAB = 1 : 40 : 10 : 0.26 : 0.05 for the CTAB-templated silica[47] and $TiCl_4$: EtOH : H_2O : F127 = 1 : 40 : 10 : 0.005 for the F127-templated titania.[46]

MTFs were deposited by dip-coating at a withdrawal speed of 1 mm s^{-1}. Once extracted from the solution, the films were subjected to a stabilization treatment consisting of consecutive 30 minute steps, comprising: exposure to 50% relative humidity (RH), thermal annealing at 60 °C and further annealing at 130 °C. Templates were eliminated by calcination at 350 °C for 2 hours, after which transparent, crack-free and homogeneous mesoporous thin films were obtained. Further details of the preparation and processing of the films are presented in the ESI.†

MPCs were prepared by successive deposition–stabilization of titania and silica films. After stabilization, the multilayer was exposed to a calcination step of 350 °C for 2 hours, in order to eliminate the template and to open the mesopore structure. To obtain MPCs with thinner layers (60–70 nm each), a 1 : 40 dilution of the original sol in ethanol was prepared. In this case, the corresponding SiO_2 and TiO_2 layers were synthesized using these dilute solutions and following the same procedures detailed above.

Reference structures were designed and synthesized by stacking the same number of SiO_2 and TiO_2 layers as their MPC counterparts, but without periodicity. These systems, labelled stacks, reproduce the total number of layers and thickness, and were used for control experiments. Stacks were produced by dip-coating successive TiO_2 layers over successively deposited SiO_2 layers (system labelled sSiTi); the thickness of each layer was either 70 nm or 110 nm, depending on the desired final structure. Stabilization and calcination steps were identical to those used for building the MPC samples.

Ag NPs were infiltrated inside the mesopore systems of the TiO_2 layers using formaldehyde as a mild reducing agent of $AgNO_3$.[44] Calcined multilayer samples were thoroughly washed in an ethanol/water solution in order to improve their accessibility. After drying, Ag NPs were synthesized inside the mesopores following the procedure detailed and sketched in Scheme S1, ESI.† The procedure leads to visible homogenous brownish colour due to the deposition of Ag NPs inside the pores of titania films, while Ag reduction in the silica films requires much longer reduction times (in the order of hours), in full agreement with previous results.[44]

Characterization

Refractive indexes and thicknesses of SiO_2 and TiO_2 mesoporous single layers and bilayers (Si substrate/SiO_2/TiO_2 and Si substrate/TiO_2/SiO_2) were measured using Spectroscopic Ellipsometry (SE SOPRA GES5A). For silica films, a Cauchy dispersion law for transparent materials was used,[28,48] while for modelling titania films, a Cauchy–Lorentz model was implemented.[49] Spectrometric Ellipsometry (SE) studies were performed on MTFs with empty pores, as well as on samples infiltrated with Ag NPs (see the ESI† for detailed empty and infiltrated sample parameters). Environmental Ellipsometric Porosimetry (EEP) measurements were also performed; water adsorption–desorption isotherms were analyzed, and pore volume and diameter were calculated using Winelli II software.[50]

UV-Vis optical characterization of the films was performed to study the SPR inside the inorganic matrices in absorbance mode in an Ocean Optics SD2000 spectrophotometer with a reflection probe. This equipment was also employed in reflection mode to study the MPC optical response.

Transmission electron microscopy (TEM) images were obtained with a JEOL JEM 1010 microscope operated at 100 kV in order to observe the pore arrays of the different systems.

Cross-sectional Scanning Electron Microscope (SEM) images were obtained for Si supported multilayered structures using a ZEISS Ultra 55 microscope to measure layer thickness.

An STEM lamella preparation was performed in order to verify the incorporation of the NPs (previously immobilized inside the mesopores using thiopyridine –HSC_5H_4N–) into the TiO_2 layers, with a focused ion beam technique using a FEI Dual Beam Helios Nanolab 650 microscope. The final thickness of the lamellas was about 20 nm and the samples were observed *in situ* with an STEM detector in dark field mode.

The film mesostructure inside the multilayer was characterized by 2D SAXS at D11A-SAXS2 line at the Laboratório Nacional de Luz Síncrotron, Campinas, SP, Brazil, using λ = 1.488 Å, a sample–detector distance of 807.8 mm, and a charge-coupled device detector (3° or 90° incidence).

Raman spectra were obtained for the incubated samples in a LabRAM HR Raman system equipped with a confocal microscope, two monochromators and a CCD detector, using the 514.5 nm line from an Ar^+ laser as the excitation source.

Modelling

A general scheme of the modelling framework and its assembly with the experimental methods is sketched in this section. A complete description of the theory employed is presented in the ESI.† The optical parameters for each single layer belonging to the SiO_2–TiO_2 MPC unit cell were obtained from the Cauchy or Cauchy–Lorentz fits of the experimental data obtained by ellipsometry conducted on monolayer and bi-layer systems. These data constitute the input for the MPCs numerical models, which were later employed to determine the layer thicknesses required to synthesize a multilayer with a specific optical response (spectral Reflectivity – R or Transmission – T). The same procedure was followed to determine the optical response of each layer and the complete MPC when pores were filled with Ag NPs.

Fig. 1 shows the synthesis-model-characterization procedure used to tune the optical properties of the multilayer. A feedback of the modelling and synthesis processes was constantly kept, leading to the accurate and reproducible design of MPC in the desired wavelength range (300 nm to 900 nm).

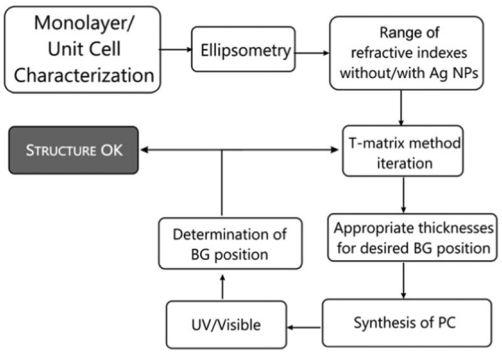

Fig. 1 Modelling-synthesis feedback scheme.

3. Results and discussion

a. Monolayer characterization

An important key to design an adequate photonic structure is to clearly determine the effective refractive index and thickness of the films, both in the case of empty matrices and in those infiltrated with the metallic NPs.

a.1. Mesoporous thin films (MTFs). SiO_2 and TiO_2 mesoporous monolayers on Si substrates were synthesized by dip coating. After the corresponding consolidation and controlled thermal treatments detailed in the Experimental section and ESI,† uniform, robust and transparent MTFs were obtained.

Spectroscopic ellipsometry (SE) was employed to determine the refractive index and thickness of the monolayers. A Cauchy model was employed to describe the optical response of SiO_2 and a Cauchy–Lorentz model was used for TiO_2 samples, in order to describe the light absorption in the UV region (see the ESI† for the details of the models used). The thicknesses obtained by this technique were consistent with the cross sectional SEM images, rendering for both single layers: $d_{SiO_2} = (112 \pm 4)$ nm and $d_{TiO_2} = (101 \pm 3)$ nm, with $n_{SiO_2} = 1.22$ and $n_{TiO_2} = (1.47 + i8 \times 10^{-3})$ at λ = 630 nm and 0%RH. Wavelength-dependent complex refractive indexes $n(\lambda) = n_r(\lambda) + in_i(\lambda)$ for both samples, obtained by best fit of the defined parameters, are plotted in Fig. 2. Note the existence of the characteristic TiO_2 absorption peak close to 300 nm in the TiO_2 extinction index.

Fig. 3 shows the TEM images of SiO_2 and TiO_2 MTFs obtained. Highly ordered and well-defined mesopores were observed in all cases. The SiO_2–CTAB thin films display a 3D-hexagonal structure with pores of around 3 nm diameter, while TiO_2–F127 films exhibit an $Im\bar{3}m$ structure with pores of *ca.* 9 nm diameter. For both types of monolayers, water adsorption–desorption curves were obtained by EEP (see the insets in Fig. 3). Monolayers presented hysteresis loops typical of mesoporous materials, which can be classified as type H1 for the silica sample and type H2 for the titania one. Using the values of film thickness and refractive index parameters of Table S1, ESI,† as seeds, an overall accessible porosity of 45% and 35% respectively was obtained. The pore and neck size distribution can be calculated from the isotherms, exhibiting pore radii of around 1.7 nm and 4.5 nm for silica and titania respectively. This result is in excellent agreement with the TEM information. In both types of films, the mesopores are interconnected by necks that ensure the diffusion of molecular or ionic species throughout the MPC, which is essential for the formation of NPs and the fast diffusion of target molecules, in the case of the Raman experiments (*vide infra*).

a.2. Ag@MTF nanocomposites. The monolayer or multilayer MTFs were loaded with controlled quantities of Ag NPs after infiltration of silver salts, followed by soft reduction with formaldehyde. The absorbance spectrum of a silver–titania NP–MTF nanocomposite after 15 min reduction is shown in Fig. S1, ESI.† A band centred at 450 nm is observed, which corresponds to the LSPR associated with metallic NPs in a dielectric medium. The peak position of the LSPR corresponds to the expected location, according to the Fröhlich condition of a silver NP surrounded by an effective dielectric medium (mesoporous TiO_2) presenting a real part of the refractive index $n_{eff}^{TiO_2}(450\ \text{nm}) = 1.57$.[51] An additional absorption term is needed to describe the ellipsometric measurements of the Ag@TiO_2 nanocomposite film, in order to fully account for the LSPR. Parameters obtained from this analysis are detailed in the ESI† (Table S1). In the case of SiO_2-CTAB, no Ag NP formation is observed at these short reduction times, as previously reported.[44] Thus, the SE parameters corresponding to mesoporous silica thin films are the same for silver infiltrated and non-infiltrated systems.

b. Modelling framework

In order to obtain the appropriate layer thicknesses of the multilayer for EM enhancement, the structure of a multilayer

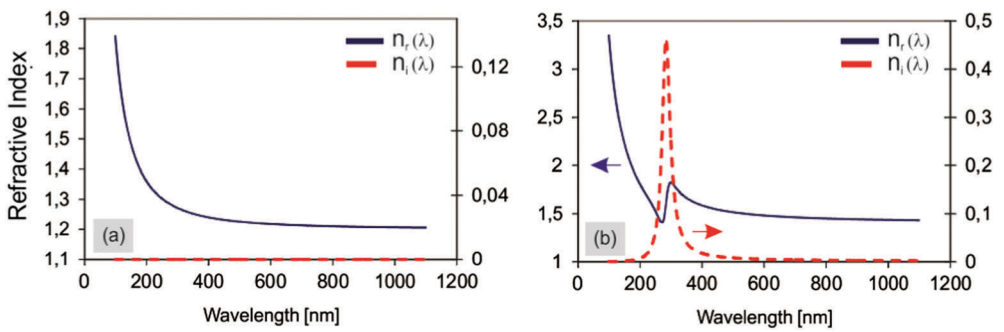

Fig. 2 Refractive index curves obtained by the ellipsometric technique. (a) SiO_2 MTF sample, (b) TiO_2 MTF sample (black solid line and left axis correspond to $n_r(\lambda)$; red dashed line and right axis correspond to $n_i(\lambda)$).

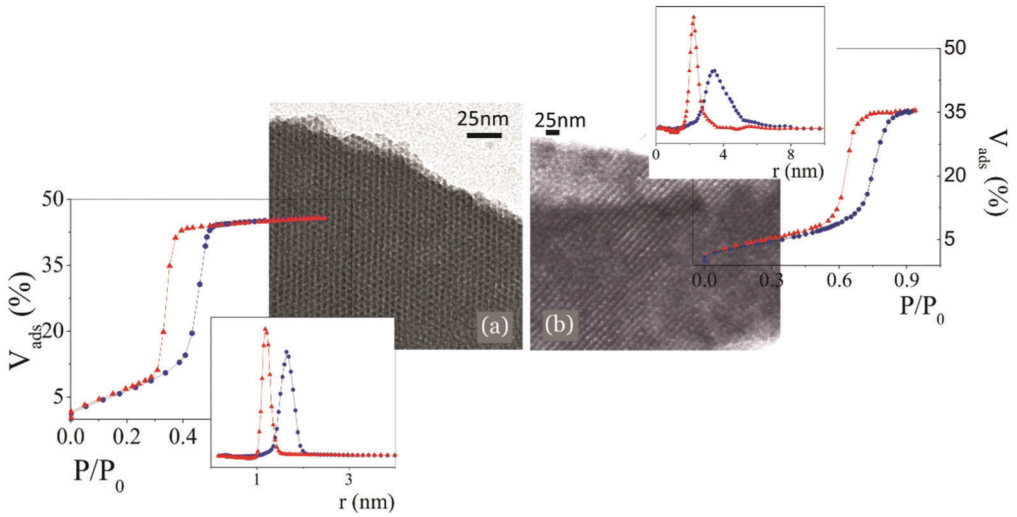

Fig. 3 TEM images of thin films: (a) SiO_2–CTAB, (b) TiO_2–F127. Insets: Water adsorption–desorption curves obtained by EEP, with the calculated pore (blue) and neck (red) radius distribution.

was modelled. An MPC multilayer structure is made up of a periodic succession of layers stacked in the z-direction as shown in Fig. S2, ESI.† In each period or unit cell, mesoporous silica and titania layers present different electric permittivities $\varepsilon_j(\lambda)$ (where $\varepsilon_j(\lambda) = [n_j(\lambda)]^2$). In all calculations, normal incidence was considered ($\theta_i = 0$), consequently no polarization distinction was necessary.

The optical response and the EM density field distribution of the multilayer structure were numerically simulated applying the transference matrix method (T-Matrix).[52] In order to simulate realistic photonic structures, the $\varepsilon_j(\lambda)$ values were those previously obtained from the SE experiments and modelling (Table S1, ESI†). The use of these parameters implies that regardless of the MPC number of layers, the refractive index of each layer is equivalent to the refractive index of the corresponding monolayer previously studied. This assumption is supported by two results:

(a) SEM images of bilayers and MPCs (see Fig. S4 and S5, ESI†) show that each layer is deposited on top of the previous one with no interpenetration, which implies a sharp interface, and permits to hypothesize that adjacent layer contamination shall be minimal or inexistent.

(b) SE measurements of thickness and refractive index values of each mesoporous layer in two and three-layer silica–titania structures (SiO_2–CTAB/TiO_2–F127 or SiO_2–CTAB/TiO_2–F127/SiO_2–CTAB) adjusted with excellent agreement with the equivalent measurements of SiO_2–CTAB (or TiO_2–F127) monolayers, obtaining optical parameters within the values included in Table S1 (ESI†).

Fig. 4a shows the simulated transmission spectrum of a 32-layered 1D MPC (unit cell composed of 70 nm thick TiO_2 and SiO_2 mesoporous layers) as a typical multilayer modelling result. The constitutive parameters of each layer were taken directly from the ellipsometry measurements described in eqn (S1)–(S3) of the ESI,† and values taken from the parameters of the pristine MTF of Table S1, ESI.† A well-defined band-gap centred at 425 nm is observed. This type of PC exhibits spatial and spectral localization and enhancement of the EM density field distribution at the band gap edges, as shown in Fig. 4(b) and (c).[1] The Bottom Edge (BE) is clearly defined at 375 nm while the Top Edge (TE) is located at 458 nm. Almost no field is present at the band gap centre (C). In addition, the EM field presents also a clear localization along the z-direction as indicated in Fig. 4(b) and (c). The EM density field distribution is localized at the SiO_2 layers in the high energy (BE) region, while it is restricted to the higher refractive index TiO_2 layers at the lower energy (TE) region of the PBG.

c. Photonic structure design: tailoring the 2D EM field localization and enhancement

Taking into consideration the field localization and enhancement properties of the PC structures described above, it is possible to design and synthesize MPCs presenting tuned PBG, the edges of which coincide with the Ag NP plasmonic band. In addition, the possibility of selectively locating Ag NPs in the titania mesopores through soft reduction (see Scheme S1, ESI†)[44] leads to a plasmon absorption located at approximately 450 nm (see the spectra of Ag@TiO_2–F127 single layers in Fig. S1, ESI†).

In this sense, the possibility of controlling the MPC band gap position along the spectrum allowed the design and synthesis of two different multilayer architectures:

(a) A structure presenting the plasmon peak position near the PBG bottom edge, from now onwards called PC-BE. In this architecture, the field enhancement is expected to be located in the SiO_2 layers. No EM enhancement derived from the PC is expected in this structure, and the EM field would therefore only be enhanced in the vicinity of the NPs, due to the SPR.

(b) A structure presenting its PBG top edge located near the plasmon wavelength, hereafter named PC-TE. In this configuration, the EM enhancement due to the PC would be confined in the TiO_2 layers (see Fig. 4), which matches with the presence of the Ag NPs plasmon. Therefore, we expect to find an EM enhancement derived from the combination of PC and plasmonic effects.

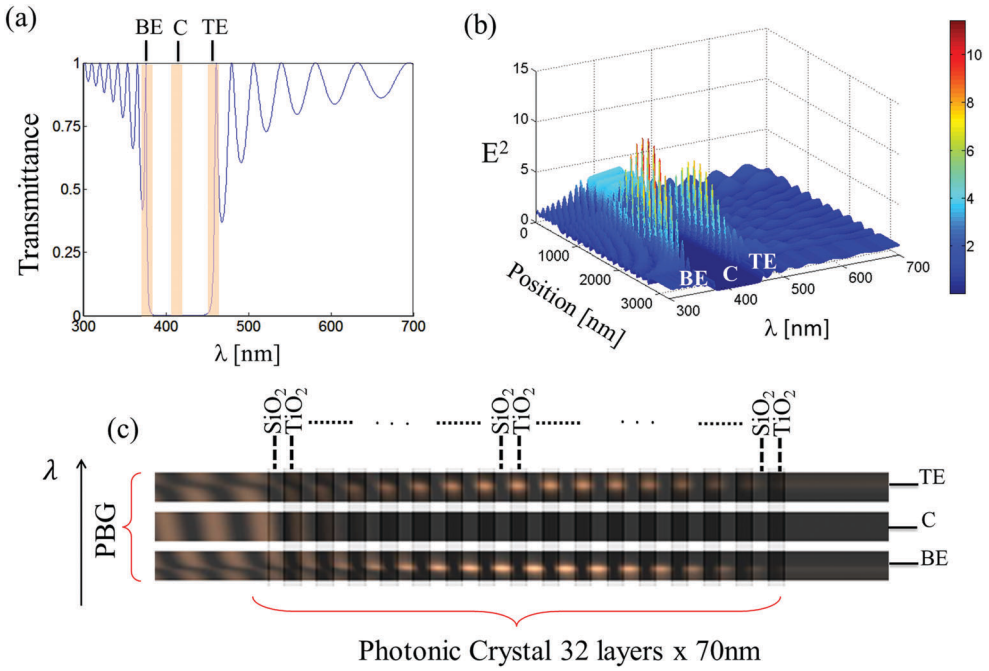

Fig. 4 (a) Transmission spectra of a 32-layered 1D-MPC of the unit cell of mesoporous SiO_2–TiO_2 thin films, (b) EM density field distribution as a function of wavelength and spatial position, (c) EM density field distribution specified for wavelengths at each band gap edge and band gap centre.

In order to design the desired NP–MPC based architectures, two MPCs were modelled using the refractive indices shown in Table S1, ESI.† Layer widths were obtained from the models, resulting in 70 nm layers for the PC-BE structure and 110 nm layers for the PC-TE structure. The multilayer architectures were synthesized following the detailed procedures described in the Experimental section and ESI.† The experimental and the modelled UV-Visible reflection spectra of the MPC without Ag NPs show a very good agreement (Fig. S4, ESI†).

Ag infiltration and reduction in multilayers takes longer times compared to monolayer films, due to the larger film thickness and pore tortuosity that hinder diffusion. For example, a typical silver adsorption step had to be experimentally modified from 15 min up to 4 h and the reduction process in the formaldehyde solution was also modified from 15 min up to 1.5 h, in order to obtain a silver content within the multilayer equivalent to the one described previously for monolayers. Taking into consideration these changes in the infiltration process, Ag NPs were selectively grown in the TiO_2–F127 layers of the MPCs. Fig. 5(a) shows an STEM image of the initial multilayers (*i.e.* before Ag infiltration). The 2D-SAXS patterns of the multilayer are shown as insets. Three distinctive diffraction rings are observable in the SAXS measurement performed at 90° incidence. The two inner ones correspond to the first and second diffraction orders of the TiO_2–F127 mesostructure, demonstrating a highly ordered mesoporous structure. The outer ring at lower distances corresponds to the SiO_2–CTAB layer. In the 3° incidence SAXS pattern, the high mesoscale order of both films is confirmed, exhibiting the typical $Im\bar{3}m$ structure for the TiO_2–F127 layer (d_{110} = 11.8 nm) and the $p6_3/mmc$ structure (d_{110} = 4.8 nm) for the SiO_2–CTAB films, in excellent agreement with previous work.[8]

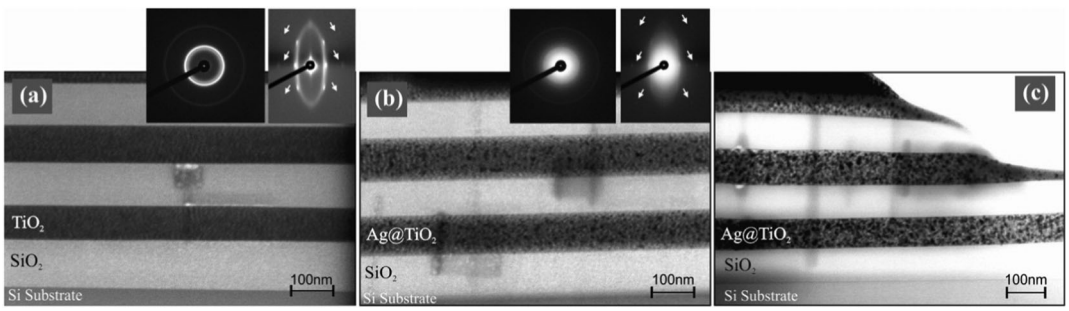

Fig. 5 STEM images of a six layer MPC: (a) MPC prior to infiltration – Insets: 2D-SAXS patterns obtained at 90° and 3° incidence (arrows indicate spots that correspond to the SiO_2 structure), (b) the same MPC after 45 min infiltration of $AgNO_3$ followed by 20 min reduction with COH_2 – Insets: 2D-SAXS patterns obtained at 90° and 3° incidence, the TiO_2–F127 signal is no longer present due to the random formation of Ag NPs, SiO_2–CTAB spots still present and unaltered, (c) sample obtained after 3 h $AgNO_3$ infiltration followed by 1.5 h reduction with COH_2.

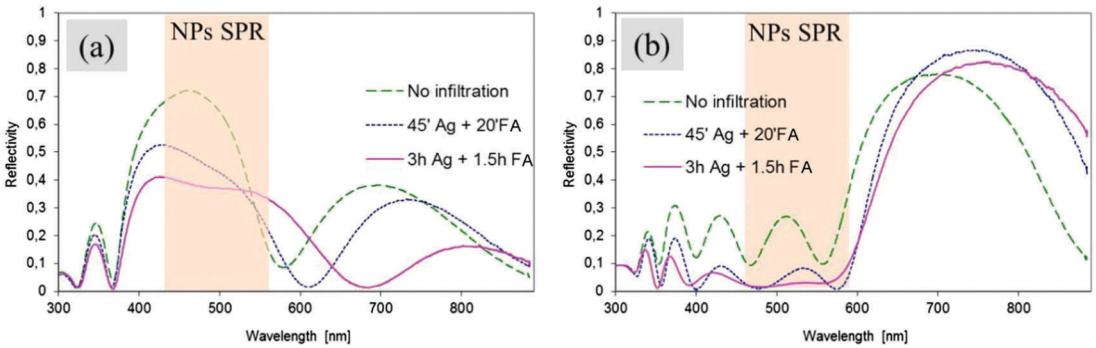

Fig. 6 Reflectance spectra for different loadings of Ag NPs varying the length of each stage of the infiltration process: (a) PC-TE structure, (b) PC-BE structure.

Fig. 5(b) and (c) show the effect of Ag infiltration followed by formaldehyde reduction on the aspect and structure of the MPC. The STEM image shown in Fig. 5(b) demonstrates the presence of silver NPs confined only within the TiO_2 layers for an intermediate loading of Ag (45 min of $AgNO_3$ infiltration followed by 20 min of formaldehyde reduction). It is important to stress the chemical selectivity attained, since no Ag NPs are observable in SiO_2–CTAB layers. This result is confirmed in the 2D-SAXS patterns, where the ring and spots that correspond to the SiO_2–CTAB mesostructure are still observable after Ag reduction, while no signal is present for the TiO_2–F127 film. In addition, a diffuse scattering at low q values, typical of a random distribution of Ag NPs in the film, is observed. Fig. 5(c) shows that at longer reduction times (after 3 h $AgNO_3$ infiltration followed by 1.5 h reduction) the titania multilayers exhibit a higher loading of Ag NPs. No Ag NPs are present in the CTAB layers after this longer treatment, reinforcing the excellent chemical selectivity of layers towards Ag infiltration. SAXS patterns of these samples (not shown) only show intense low q scattering, as found in similar systems.[44] By analyzing the STEM images of Fig. 5(b) and (c), a higher number of Ag centres are observed, which also show an increase in the average diameter from (4.9 ± 0.8) nm up to (6.7 ± 0.7) nm (see Fig. S5, ESI†).

Fig. 6 displays the different reflectivity spectra obtained for PC-BE and PC-TE structures with the different loadings of Ag NPs. It is possible to observe a reduction of the reflectivity (in the zone denoted with a shaded strip) in the spectra of both structures due to the absorption of the LSPR. The performed spectroscopies show that these results are in very good agreement with the predictions of the model with regard to the PBG widening and flattening. However, it can be noted that in the case of the PC-TE, the superposition of the PC reflectivity and the plasmon flattens out the reflectivity signal. In the case of the PC-BE structure, pore filling with the NPs results in a bathochromic shift of the PC band edge reflectivity with reduction time.

d. Probing of the EM field inside the photonic structure

MPCs present highly accessible porosity, which ensures an easy diffusion of a variety of molecules in the mesopore systems. This constitutes an advantage for the design of sensors based in the pre-concentration of molecules which are subjected to amplified fields that enhance their signal (*e.g.*, SERS).[34–36] We exploit this unique feature of mesoporous materials by using Raman-active molecules as spectroscopic probes, in order to study the EM field inside the nanoparticle-loaded MPC. Thiopyridine (HSC_5H_4N), which bonds to the Ag NP *via* the thiol group, was selected as the probe molecule to study the EM enhancement due to the combined plasmonic and photonic effects inside the designed structures. The Raman signals of the probe molecules adsorbed inside the pores of MPCs and in the corresponding stacks were compared to assess for the effect of the field enhancement due to the photonic structure.

In order to distinguish the EM enhancement due to the PC structure from that associated with the NP plasmons, two non-periodic structures, formed by SiO_2–TiO_2 stacks, were also designed, synthesized and infiltrated with NPs, as described in Section 2. These stacks present the same total thickness, SiO_2/TiO_2 ratio and the same average number of NP per unit volume as the PC-TE and PC-BE structures, but no periodicity. Due to their lack of periodicity, these stacks do not present PBG, and the corresponding EM enhancement due to the PC is not expected. Consequently, given that the average number of NPs included in both structures is the same, a comparison of the Raman signal between the Ag@MPC and the Ag@stack samples allows identifying the effect of MPCs in the Raman signal enhancement.

The stacked systems (labelled sSiTi) were prepared by successive dip-coating of TiO_2 layers over SiO_2 layers, attaining a total final thickness equivalent to the MPC (see SEM images Fig. S6b and d, ESI†). Fig. S6a and c, ESI† show the reflectivity spectra of the synthesized stack samples, displaying the experimental data obtained, together with the numerical modelling results. A very good agreement between the experimental and models was attained.

Probe molecules were infiltrated inside the mesoporous samples by immersion of the films in 10 μM thiopyridine solution inside covered Petri dishes in order to maintain the solution concentration, under constant stirring for 4 h. Subsequently, samples were withdrawn from the solution and allowed to dry under ambient conditions. Incubation and Raman analysis were performed only on samples infiltrated for 45 min with

$AgNO_3$(0.1 M) + 20 min with CH_2O (7%), which ensures an adequate NP loading degree (as shown in Fig. 5b), as well as enough accessibility for the thiopyridine molecules.

Fig. 7a shows the obtained Raman spectra (irradiation at 514.5 nm) for the PC-TE structure infiltrated with Ag NPs and incubated with thiopyridine for 4 h (10 μM) compared to the corresponding stack (sSiTi-TE). As previously mentioned, the MPC and the stack samples were infiltrated and incubated simultaneously and consequently they present the same average Ag and thiopyridine content. The spectrum corresponding to the MPC sample displays a noticeable more intense Raman signal. This result is consistent with the enhancement expected, due to the combined effects of the PC and the Ag SPR. In particular, the additional enhancement present in the tuned MPC allowed a distinct identification of four thiopyridine spectral lines (associated with the ring breathing – 1013 cm^{-1} and 1069 cm^{-1}, the C–S stretching mode – 1100 cm^{-1} and the characteristic $\beta_{(CH)}$ mode – 1222 cm^{-1}). Conversely, the signal measured for the corresponding non-periodic stacks results lower in intensity, with most of the peaks hidden in the background noise. The MPC Raman signal in Fig. 7a evidences an enhancement of 1.8–2.2× (measured @1100 cm^{-1}) with respect to the sSiTi-TE Raman spectra. Considering that the only difference between the PC-TE sample and the corresponding stack is the periodicity of the PC, the obtained results confirm the interplay between the photonic and plasmonic responses in this system.

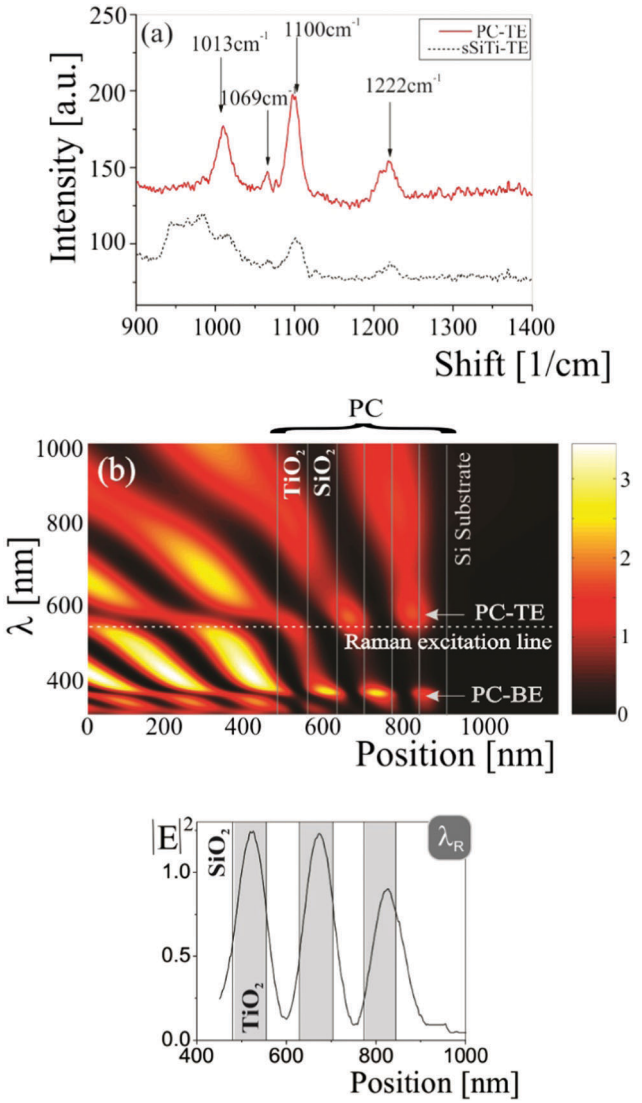

Fig. 7 (a) Thiopyridine Raman signal of Ag@PC-TE and Ag@sSiTi-TE (6 layers of 70 nm each); (b) EM density field distribution for the Ag@PC-TE structure. Inset: EM density profile for λ_R.

These results can be readily interpreted resorting to calculations. Fig. 7b shows the density field distribution simulation associated exclusively with the PC enhancement, for the Ag@PC-TE structure. As shown in Fig. 6a, the incorporation of Ag NPs results in a flattening and widening of the PC band gap. These effects make the definition of the BG edge somehow difficult, since they extend for several nm, as can be seen in the reflectivity signals of Fig. 6. To correctly define the top edge, the density field distribution map of Fig. 7b is useful, since it denotes a clear PC enhancement in Ag@TiO_2 layers around 550 nm. This enhancement overlaps with the tail of the LSPR signal (see Fig. S1, ESI†). The Raman excitation line at λ_R = 514.5 nm is included in the overlapping region.

Previous works[53] have shown that the Raman signal depends on the incident light and on the enhanced resonance Raman cross section spectrum. This factor in turn depends on the cross section of the probe molecule free from the surface enhancement and on the wavelength of the NP SPR, and is therefore independent of the incident field. The Raman signal observed in SERS originates in the enhanced field at the vicinity of the surface of the NP, where the probe molecules are adsorbed. Since the enhanced Raman cross sectional spectrum does not depend on the incident field, the enhancement due to the NP's SPR is expected to be the same in the periodic (Ag@PC-TE) and non-periodic (Ag@sSiTi-TE) structures presented here, given they both contain the same average number of NPs per unit volume. It is therefore clear that the increase in the Raman signal observed in Fig. 7 is related to the EM enhancement produced by the periodicity of the MPC. This enhanced field is confined in areas more than two orders of magnitude larger than the NP (Fig. 7b), and therefore acts as the incident field to the NP.

This suggests that the enhanced Raman signal observed in Ag@PC-TE, compared to that of Ag@sSiTi-TE, is due to the enhancement of the EM field incident on the NP (originated in the periodicity of the structure), while the enhancement associated with the NP plasmons is the same for both the structures. Congruently, the simulated EM density field distribution for the Ag@PC-TE shown in Fig. 7b predicts a factor 2 enhancement in Ag@TiO_2 layers with respect to the EM field in the adjacent SiO_2 layers which is consistent with the amplification observed in the Raman signal in Fig. 7a. This factor and the EM confinement in the TiO_2 layers at the Raman excitation line (λ_R) are clearly observable in the Fig. 7 inset. At this wavelength, which almost coincides with the TE band gap location (λ_{TE}), the EM intensity maxima are coincident with the TiO_2 layers.

It can be then concluded that the system presented here shows photonic–plasmonic coupling, which leads to the obtainment of SERS-active substrates.

On the other hand, the PC-BE structure studied shows somewhat counterintuitive results. In the originally designed PC-BE multilayer, the field concentration was expected to be in the silica layers, which do not contain the Ag NPs; therefore, the absence of combined effects of the PC periodicity and the plasmon response of the Ag NPs SPR was expected. Fig. 8a clearly shows an increase of the Raman signal for the multilayer with respect to the sSiTi-BE stack structure of about 4–5 times (measured @1100 cm^{-1}). In order to clarify this unexpected behaviour we performed numerical simulations of the density field distribution for this structure, as presented in Fig. 8b. This figure evidences an EM field enhancement of about 3.5–4× measured in the SiO_2 layers at the BE of the BG, where no NPs are present (see the STEM images in Fig. 5). Once again, the MPC enhancement can be separated from the SPR one (the former acting on the field incident to the NP and the latter on the field localized in the vicinity of its surface) and the numerical simulations result in good agreement with the Raman enhancement obtained due to the PC. However, these results are not the expected ones. It is possible to observe that the spatial confinement of the EM field is not perfect, with some enhanced EM field spreading out to the adjacent TiO_2 layers where NPs have been adsorbed.

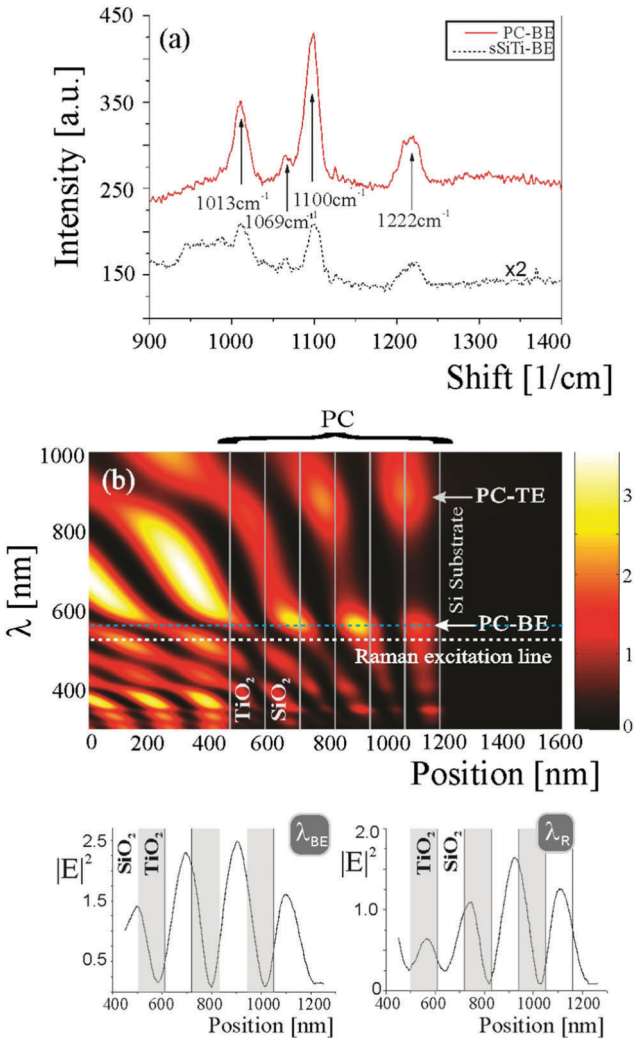

Fig. 8 (a) Thiopyridine Raman signal of Ag@PC-BE. (b) EM density field distribution for the Ag@PC-BE structure. Insets: The EM density profile for λ_{BE} and λ_R.

This EM "spill over" might be caused by a combination of effects. On one hand, while a six-layer structure was proven to be enough to develop distinct PBG with reflectivity between 75 and 90% (Fig. 6), the configuration is not enough to permit to fully localize the EM field in the desired silica layers. This effect causes the EM maxima at λ_{BE} to be slightly shifted spatially towards TiO_2 layers as shown in the calculations (see the left inset of Fig. 8b). Consequently, the thiopyridine molecules adsorbed in Ag NPs in the TiO_2 layers near the interfaces are excited, combining the enhancement effects of the Ag NPs and of the PC. On the other hand, as the PC-BE layers are slightly thicker than the ones in the PC-TE structure (a requirement for tuning the band gap), they are likely to contain higher amounts of Ag and thiopyridine. One final factor that might influence this result is the small shift in the Raman excitation line (λ_R) with respect to the BE band gap location (λ_{BE}). This proximity may cooperate to tune and excite the Ag NPs in the vicinity of the TiO_2–SiO_2 interface, as shown in the EM density field in the right inset of Fig. 8b, where maxima are located near the layer interfaces. Therefore, the EM field can penetrate at least partially in the titania mesoporous layers. As a consequence, even though most of the EM enhancement is not localized in the TiO_2 layers but in the SiO_2 ones, at the Raman excitation (λ_R) the EM field can penetrate the adjacent TiO_2 layers containing significant amounts of NP and thiopyridine, accounting for the observed Raman enhancement. Interestingly, this MPC-based nanocomposite also presents potential interest as a SERS-active detection system. This example shows that although an *a priori* rational design of a coupled photonic–plasmonic device can be useful for obtaining extra Raman enhancements, a complete modelling and analysis of the optical system is necessary to fully understand the observed results, which may be counterintuitive and lead to higher enhancements.

4. Conclusions

In this contribution, we present a robust method to design and synthesize a complex MPC–NP nanocomposite with predetermined optical response, and accessible to probe molecules. The proposed structure corresponds to a mesoporous multilayer composed of a TiO_2/SiO_2 unit cell. A selective mild reduction process permits to arbitrarily synthesize Ag NPs only within the TiO_2 pores. This nanocomposite presents hierarchical and highly tunable properties: the refractive index periodicity at the nanometric scale permits to tune the optical response, including the PBG and the position of the band edges, the selection of the metallic NP permits to tune these features with the SPR band, while the porosity at the mesoscale ensures molecular accessibility and favours vapour condensation.

The optical properties were carefully tailored through the feedback between synthesis, spectrophotometry and spectrometric ellipsometry measurements and a theoretical approach. Each layer of the unit cell was fully characterized, permitting us to obtain not only the effective refractive index of the mesoporous SiO_2 and TiO_2 layers, but also the effective refractive index for TiO_2 layers containing Ag NPs selectively located inside its pores.[44] The combination of experimental results and the effective medium model gives accurate refractive indices for these nanocomposites, taking into consideration that the elements inside the inorganic matrices (in this case Ag NPs inside TiO_2 layers) accomplish the condition $r \ll \lambda$ (where r represents the average radius of the NPs).

We have thus shown that by using a simple but very robust model for the optical response of the photonic crystal (which employs experimental information obtained for each unit cell), it is possible to model and predict the reflectivity of complex structures that combine photonic and plasmonic properties. With these tools, we were able to design adequate MPCs which allowed the spectral and spatial confinement of the EM field. Taking into consideration this dual localization, photonic/plasmonic structures were tailored to tune the EM photonic enhancement with the periodicity of the 1D photonic crystals. In principle, this method can be adapted to the great available variety of mesoporous oxides and metallic NPs, leading to a tailorable platform to study the interplay between photonic and plasmonic systems.

Raman spectroscopy was successfully used as a tool for probing the EM field within the photonic–plasmonic platforms. The obtained increased Raman signals validate the theoretical results, showing a clear EM field enhancement due to the periodic stratification in comparison with non-periodic stack structures. As a consequence, the observed PC-assisted enhanced Raman response opens the path to using these nano-systems as SERS-based sensors. The obtained results confirm that periodicity is a promising mechanism for field enhancement that can indeed be used to improve their qualities. Finally, the leakage of the EM density field from SiO_2 to TiO_2 gives rise to another enhancement which is also a consequence of periodic stratification.

In conclusion, the combination of an adequate and simple prediction theory with robust experimental methods is the sound basis of a platform for the rational design of new nanostructures which can lead to the development of smart plasmonic–photonic devices with diverse applications in sensors, optoelectronics or energy collection.

Acknowledgements

Funding was provided by ANPCyT (PICT #0985-2010, #2087-2012, #1167-2012, #3526-2015), UBACyT (20020100100636, 20020130100610BA), CONICET (PIP 00186) and ABT-Lus for access to the LNLS SAXS1 beamline (project SAXS1-11060). Dr Paula Angelomé is acknowledged for TEM images and Dr Emilia Halac for Raman spectra. R. M. G. especially acknowledges Eduardo D. Martínez for collaborative discussions. M. B., G. J. A. A. S.-I., M. C. F. and M. L. M. R. are members of CONICET. G. J. A. A. S.-I. is a member of Gabbo's.

References

1 J. D. Joannopoulos, S. G. Johnson, J. N. Winn and R. D. Meade, *Photonic crystals: molding the flow of light*, Princeton university press, 2011.
2 B. Auguié, M. C. Fuertes, P. C. Angelomé, N. López Abdala, G. J. A. A. Soler-Illia and A. Fainstein, *ACS Photonics*, 2014, **1**, 775–780.
3 R. M. Almeida and A. S. Rodrigues, *J. Non-Cryst. Solids*, 2003, **326–327**, 405–409.
4 O. Sánchez-Sobrado, M. E. Calvo and H. Míguez, *J. Mater. Chem.*, 2010, **20**, 8240–8246.
5 M. Stefik, S. Guldin, S. Vignolini, U. Wiesner and U. Steiner, *Chem. Soc. Rev.*, 2015, **44**, 5076–5091.
6 A. C. Edrington, A. M. Urbas, P. DeRege, C. X. Chen, T. M. Swager, N. Hadjichristidis, M. Xenidou, L. J. Fetters, J. D. Joannopoulos, Y. Fink and E. L. Thomas, *Adv. Mater.*, 2001, **13**, 421–425.
7 S. Y. Choi, M. Mamak, G. von Freymann, N. Chopra and G. A. Ozin, *Nano Lett.*, 2006, **6**, 2456–2461.
8 M. C. Fuertes, F. J. López-Alcaraz, M. C. Marchi, H. E. Troiani, V. Luca, H. Míguez and G. d. A. Soler-Illia, *Adv. Funct. Mater.*, 2007, **17**, 1247–1254.
9 H. Floch, J.-J. Priotton and I. M. Thomas, *Thin Solid Films*, 1989, **175**, 173–178.
10 M. E. Calvo, O. Sánchez-Sobrado, S. Colodrero and H. Míguez, *Langmuir*, 2009, **25**, 2443–2448.
11 D.-L. Guo, L.-X. Fan, F.-H. Wang, S.-Y. Huang and X.-W. Zou, *J. Phys. Chem. C*, 2008, **112**, 17952–17956.
12 J. J. Steele, A. C. van Popta, M. M. Hawkeye, J. C. Sit and M. J. Brett, *Sens. Actuators, B*, 2006, **120**, 213–219.
13 P. Yang, D. Zhao, D. I. Margolese, B. F. Chmelka and G. D. Stucky, *Nature*, 1998, **396**, 152–155.
14 D. Grosso, F. Cagnol, G. d. A. Soler-Illia, E. L. Crepaldi, H. Amenitsch, A. Brunet-Bruneau, A. Bourgeois and C. Sanchez, *Adv. Funct. Mater.*, 2004, **14**, 309–322.
15 G. J. A. A. Soler-Illia, P. C. Angelomé, M. C. Fuertes, A. Calvo, A. Wolosiuk, A. Zelcer, M. G. Bellino and E. D. Martínez, *J. Sol-Gel Sci. Technol.*, 2011, **57**, 299–312.
16 S. Guldin, M. Kolle, M. Stefik, R. Langford, D. Eder, U. Wiesner and U. Steiner, *Adv. Mater.*, 2011, **23**, 3664–3668.
17 M. C. Fuertes, S. Colodrero, G. Lozano, A. R. González-Elipe, D. Grosso, C. Boissiere, C. Sanchez, G. J. d. A. Soler-Illia and H. Míguez, *J. Phys. Chem. C*, 2008, **112**, 3157–3163.
18 Y. Dou, J. Han, T. Wang, M. Wei, D. G. Evans and X. Duan, *J. Mater. Chem.*, 2012, **22**, 14001–14007.
19 M. Ghazzal, O. Deparis, A. Errachid, H. Kebaili, P. Simonis, P. Eloy, J.-P. Vigneron, J. De Coninck and E. M. Gaigneaux, *J. Mater. Chem.*, 2012, **22**, 25302–25310.
20 M. N. Ghazzal, O. Deparis, J. De Coninck and E. M. Gaigneaux, *J. Mater. Chem. C*, 2013, **1**, 6202–6209.

21 N. Hidalgo, M. E. Calvo, M. G. Bellino, G. J. A. A. Soler-Illia and H. Míguez, *Adv. Funct. Mater.*, 2011, **21**, 2534–2540.

22 M. E. Calvo, N. Hidalgo, R. Schierholz, A. Kovacs, A. Fernandez, M. G. Bellino, G. J. A. A. Soler-Illia and H. Miguez, *Nanoscale*, 2015, **7**, 16583–16589.

23 R. Li, M. Faustini, C. Boissière and D. Grosso, *J. Phys. Chem. C*, 2014, **118**, 17710.

24 G. J. A. A. Soler-Illia and P. Innocenzi, *Chem. – Eur. J.*, 2006, **12**, 4478–4494.

25 S. Besson, T. Gacoin, C. Ricolleau and J.-P. Boilot, *Chem. Commun.*, 2003, 360–361.

26 M. D. Pérez, E. Otal, S. A. Bilmes, G. J. Soler-Illia, E. L. Crepaldi, D. Grosso and C. Sanchez, *Langmuir*, 2004, **20**, 6879–6886.

27 V. Sánchez, E. Martínez, M. Martínez Ricci, H. Troiani and G. Soler-Illia, *J. Phys. Chem. C*, 2013, **117**, 7246–7259.

28 A. Fischereder, M. L. Martinez-Ricci, A. Wolosiuk, W. Haas, F. Hofer, G. Trimmel and G. J. Soler-Illia, *Chem. Mater.*, 2012, **24**, 1837–1845.

29 S. Besson, T. Gacoin, C. Ricolleau, C. Jacquiod and J.-P. Boilot, *Nano Lett.*, 2002, **2**, 409–414.

30 S. Colodrero, A. Mihi, L. Häggman, M. Ocana, G. Boschloo, A. Hagfeldt and H. Miguez, *Adv. Mater.*, 2009, **21**, 764–770.

31 D. P. Puzzo, F. Scotognella, M. Zavelani-Rossi, M. Sebastian, A. J. Lough, I. Manners, G. Lanzani, R. Tubino and G. A. Ozin, *Nano Lett.*, 2009, **9**, 4273–4278.

32 L. D. Bonifacio, D. P. Puzzo, S. Breslav, B. M. Willey, A. McGeer and G. A. Ozin, *Adv. Mater.*, 2010, **22**, 1351–1354.

33 K. S. Lee and M. A. El-Sayed, *J. Phys. Chem. B*, 2006, **110**, 19220–19225.

34 A. Wolosiuk, E. D. Martínez, N. G. Tognalli, M. Granada, M. C. Fuertes, H. Troiani, S. A. Bilmes, A. Fainstein and G. J. A. A. oler-Illia, *ACS Appl. Mater. Interfaces*, 2014, **6**, 5263–5272.

35 V. Lopez-Puente, S. Abalde-Cela, P. C. Angelome, R. A. Alvarez-Puebla and L. M. Liz-Marzan, *J. Phys. Chem. Lett.*, 2013, **4**, 2715–2720.

36 V. López-Puente, P. C. Angelomé, G. J. A. A. Soler-Illia and L. M. Liz-Marzán, *ACS Appl. Mater. Interfaces*, 2015, **7**, 25633–25640.

37 P. Xu, L. Kang, N. H. Mack, K. S. Schanze, X. Han and H.-L. Wang, *Sci. Rep.*, 2013, **3**, 2997.

38 Z. Zhang, L. Zhang, M. N. Hedhili, H. Zhang and P. Wang, *Nano Lett.*, 2013, **13**, 14–20.

39 Z. Jin, Q. Wang, W. Zheng and X. Cui, *ACS Appl. Mater. Interfaces*, 2016, **8**, 5273–5279.

40 O. Sánchez-Sobrado, G. Lozano, M. E. Calvo, A. Sánchez-Iglesias, L. M. Liz-Marzán and H. Míguez, *Adv. Mater.*, 2011, **23**, 2108–2112.

41 F. García-Santamaría, V. Salgueiriño-Maceira, C. López and L. M. Liz-Marzán, *Langmuir*, 2002, **18**, 4519–4522.

42 E. D. Martínez, M. G. Bellino and G. J. A. A. Soler-Illia, *ACS Appl. Mater. Interfaces*, 2009, **1**, 746–749.

43 E. D. Martínez, L. Granja, M. G. Bellino and G. J. A. A. Soler-Illia, *Phys. Chem. Chem. Phys.*, 2010, **12**, 14445–14448.

44 M. C. Fuertes, M. Marchena, M. C. Marchi, A. Wolosiuk and G. J. A. A. Soler-Illia, *Small*, 2009, **5**, 272–280.

45 C. J. Brinker, Y. Lu, A. Sellinger and H. Fan, *Adv. Mater.*, 1999, **11**, 579–585.

46 E. L. Crepaldi, G. J. d. A. Soler-Illia, D. Grosso, F. Cagnol, F. Ribot and C. Sanchez, *J. Am. Chem. Soc.*, 2003, **125**, 9770–9786.

47 D. Grosso, A. R. Balkenende, P. A. Albouy, A. Ayral, H. Amenitsch and F. Babonneau, *Chem. Mater.*, 2001, **13**, 1848–1856.

48 H. G. Tompkins and W. A. McGahan, *Spectroscopic ellipsometry and reflectometry: a user's guide*, Wiley, New York, 1999.

49 A. B. Djurišic and E. H. Li, *Appl. Opt.*, 1998, **37**, 5291–5297.

50 C. Boissiere, D. Grosso, S. Lepoutre, L. Nicole, A. B. Bruneau and C. Sanchez, *Langmuir*, 2005, **21**, 12362–12371.

51 U. Kreibig and M. Vollmer, *Optical Properties of Metal Clusters*, Springer, Berlin, 1995.

52 P. Yeh, A. Yariv and C.-S. Hong, *J. Opt. Soc. Am.*, 1977, **67**, 423–438.

53 K.-i. Yoshida, T. Itoh, V. Biju, M. Ishikawa and Y. Ozaki, *Phys. Rev. B: Condens. Matter Mater. Phys.*, 2009, **79**, 085419.